Article

Internally hollow Cu$_2$O nanoframes with the abundance of {110} facets enhance direct propylene epoxidation

Yueming Qiu[1,5], Yichen Zhang[1,5], Ronghui Zhang[1], Meng Huang[1], Kok Bing Tan[1,2], Guowu Zhan [2], Gang Fu [1,3] ✉, Qingbiao Li [1,4] ✉ & Jiale Huang [1] ✉

The gas-phase direct epoxidation of propylene (DEP) using molecular oxygen, which has been deemed the 'dream reaction' for propylene oxide (PO) production due to its efficiency and environmental benefits, remains highly regarded by researchers. In this contribution, we engineer a series of Cu$_2$O nanocatalysts by employing the ligand-protection/selective facet-etching technique. Among these, the internally hollow Cu$_2$O nanoframes, featuring increased specific surface area and a prevalence of {110} sites, achieve a triple-win in activity, selectivity, and stability, with an optimal PO formation rate of 0.18 mmol g$_{cat}^{-1}$ h^{-1} and a selectivity of 83.8% at 175 °C. In addition, long-term tests confirm that these internally hollow nanoframes maintain high activity and selectivity for over 300 minutes. Further characterizations, combined with density functional theory calculations, confirm that the unique atomic arrangement of copper and oxygen on the Cu$_2$O {110} facet facilitate the formation of chemically adsorbed oxygen species and propylene oxide as well. We anticipate that the ligand-protection/selective facet-etching approach may serve as a versatile method for fabricating well-defined catalyst architectures.

The selective catalytic conversion of propylene (C$_3$H$_6$) into propylene oxide (PO) is an important process in the field of industrial catalysis[1–3]. PO serves as a bulk chemical feedstock for the manufacture of versatile value-added chemicals, which are essential in sectors of microchip and capital construction fields[4–6]. Market research data forecasts that the annual demand of PO will surpass 20 million tons in 2025[7,8]. However, conventional industrial methods for PO production are encumbered by their cost-ineffectiveness and adverse environmental impact, resulting in the generation of multiple by-products that intricately complicate downstream separation processes. To address this challenge, the direct epoxidation of propylene (DEP) with molecular oxygen has emerged as an ideal alternative for the 21st century, owing to its promise of achieving 100% theoretical atom economy and a sustainable, environmentally friendly process[8–12].

The DEP reaction using Cu-based catalysts, especially Cu$_2$O nanocrystals, has been the subject of intensive research[9,11,13–15]. Various Cu$_2$O nanostructures, such as nanocubes, octahedra, and rhombic dodecahedra, along with their modified counterparts, have been synthesized, yielding significant understanding of the influence of crystallographic orientation on catalytic outcomes[16,17]. The different Cu$_2$O facets, such as {111}, {100} and {110}, with different surface oxygen coordination structures, are closely associated with the production propensity for acrolein, CO$_2$, and PO, respectively[9,11]. However, the PO yield was not satisfactory due to the low density of the active site and the limited specific surface areas on the Cu$_2$O catalysts. The synthesis of hollow Cu$_2$O nanoframes has been identified as a promising solution to overcome the existing challenges, primarily due to their enhanced surface-to-volume ratio and

[1]Department of Chemical and Biochemical Engineering, College of Chemistry and Chemical Engineering, Xiamen University, Xiamen, Fujian, China. [2]College of Chemical Engineering, Integrated Nanocatalysts Institute (INCI), Huaqiao University, Xiamen, China. [3]State Key Laboratory of Physical Chemistry of Solid Surfaces, Xiamen University, Xiamen, Fujian, China. [4]College of Ocean Food and Biology Engineering, Jimei University, Xiamen, Fujian, China. [5]These authors contributed equally: Yueming Qiu, Yichen Zhang. ✉e-mail: gfu@xmu.edu.cn; kelqb@xmu.edu.cn; cola@xmu.edu.cn

improved substrate transfer capacity[3,18,19]. Specifically designed hollow Cu$_2$O nanoframes, with a focus on exposing preferred crystallographic planes, were expected to demonstrate superior catalytic performance. For example, Sui et al.[20] revealed that hollow Cu$_2$O catalysts with {111} edge sites significantly surpassed their solid counterparts in the oxidative degradation of pollutants. In addition, hollow Cu$_2$O nanoframes, characterized by {111} edge sites, exhibited enhanced catalytic performance in photocatalysis reactions as compared with conventional Cu$_2$O cubes[21–25]. However, the indiscriminate formation of diverse exposed facets did not improve the

efficiency of the DEP reaction, owing to the critical dependence of propylene oxide (PO) production on the exposure of the {110} facets of Cu$_2$O. Therefore, there is an urgent need to develop synthetic methods specifically aimed at selectively engineering Cu$_2$O nanoframes to prioritize the exposure of {110} facets.

In this work, the fabrication of hollow Cu$_2$O nanoframes with abundant {110} facets was made possible through an innovative synthesis approach called ligand-protection/selective facet-etching. This was achieved by employing lauryl sodium sulfate as a ligand protecting agent for preferentially binding to the high-surface-energy
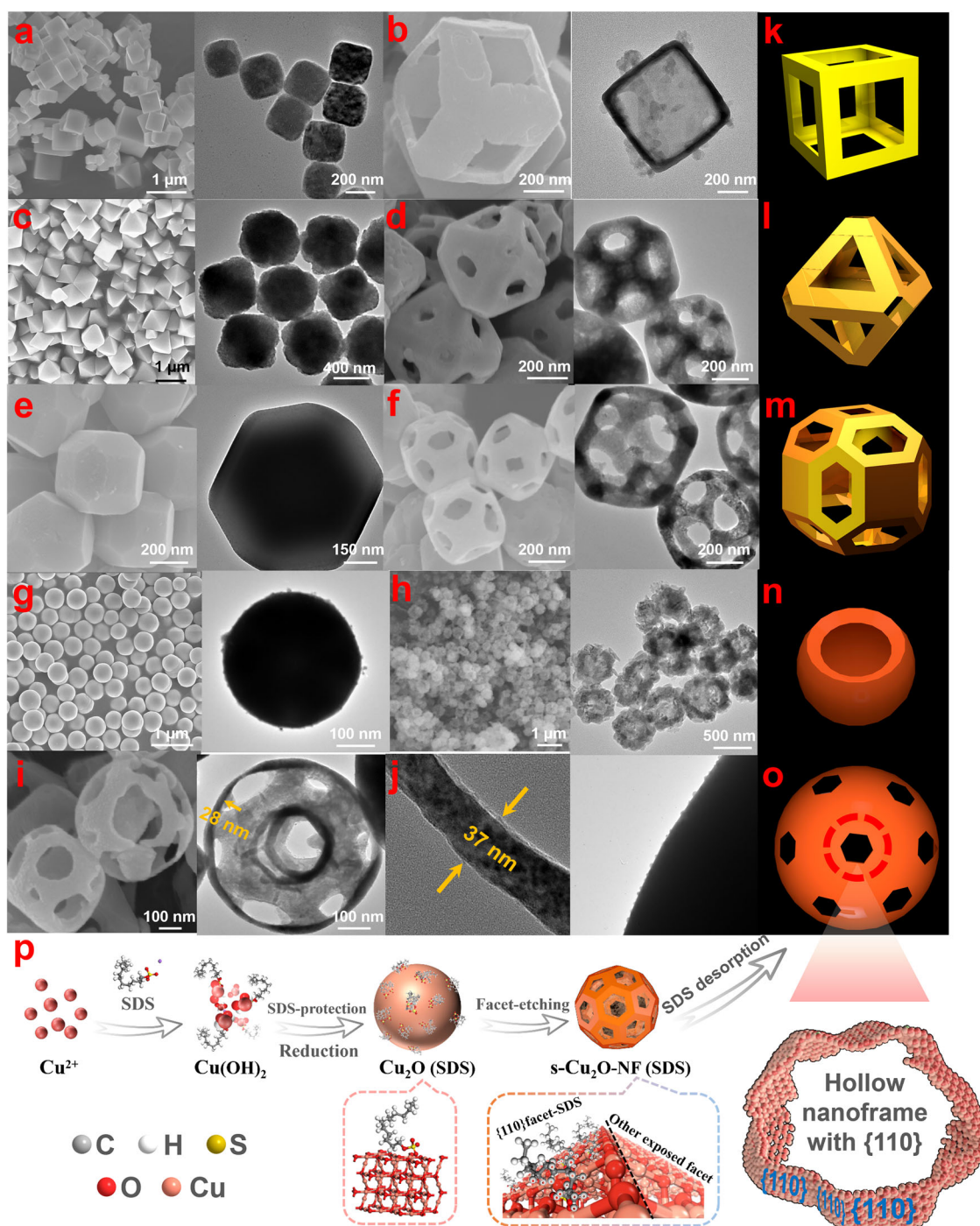

Fig. 1 | Microscopic characterizations and schematic illustration. SEM and TEM images of (**a**) c-Cu$_2$O, (**b**) c-Cu$_2$O-NF, (**c**) o-Cu$_2$O, (**d**) o-Cu$_2$O-NF, (**e**) d-Cu$_2$O, (**f**) d-Cu$_2$O-NF, (**g**) s-Cu$_2$O, (**h**) s-Cu$_2$O-NC and (**i, j**) s-Cu$_2$O-NF. Three-dimensional structure models of (**k**) c-Cu$_2$O-NF, (**l**) o-Cu$_2$O-NF, (**m**) d-Cu$_2$O-NF, (**n**) s-Cu$_2$O-NC and (**o**) s-Cu$_2$O-NF models. **p** Schematic illustration for the synthesis process of s-Cu$_2$O-NF.
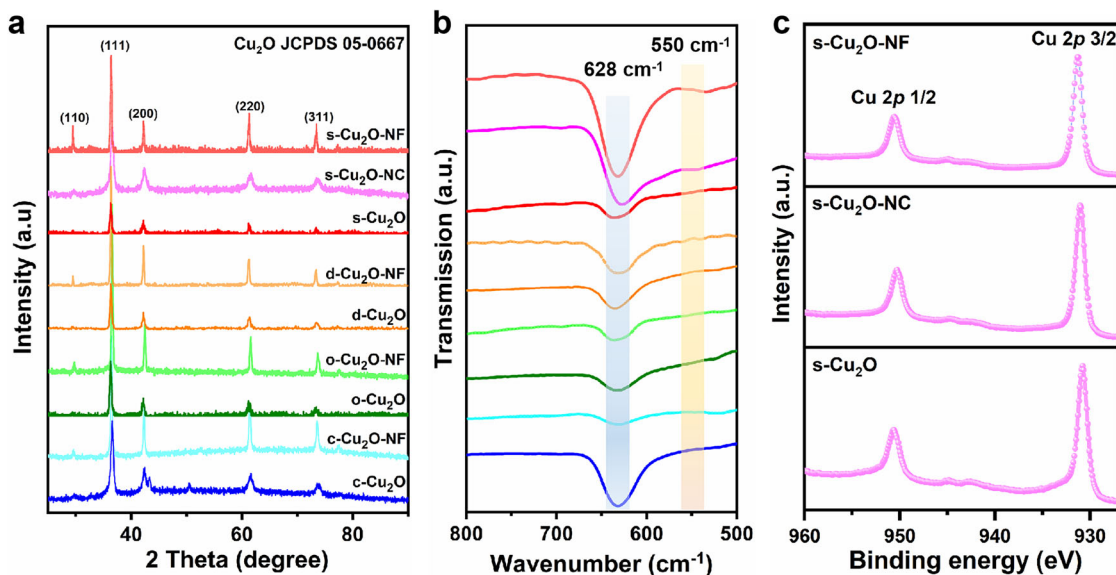
Fig. 2 | Structural characterizations. (**a**) XRD and (**b**) FT-IR patterns of as-prepared Cu_2O nanocatalysts. **c** XPS patterns of Cu of s-Cu_2O, s-Cu_2O-NC and s-Cu_2O-NF.
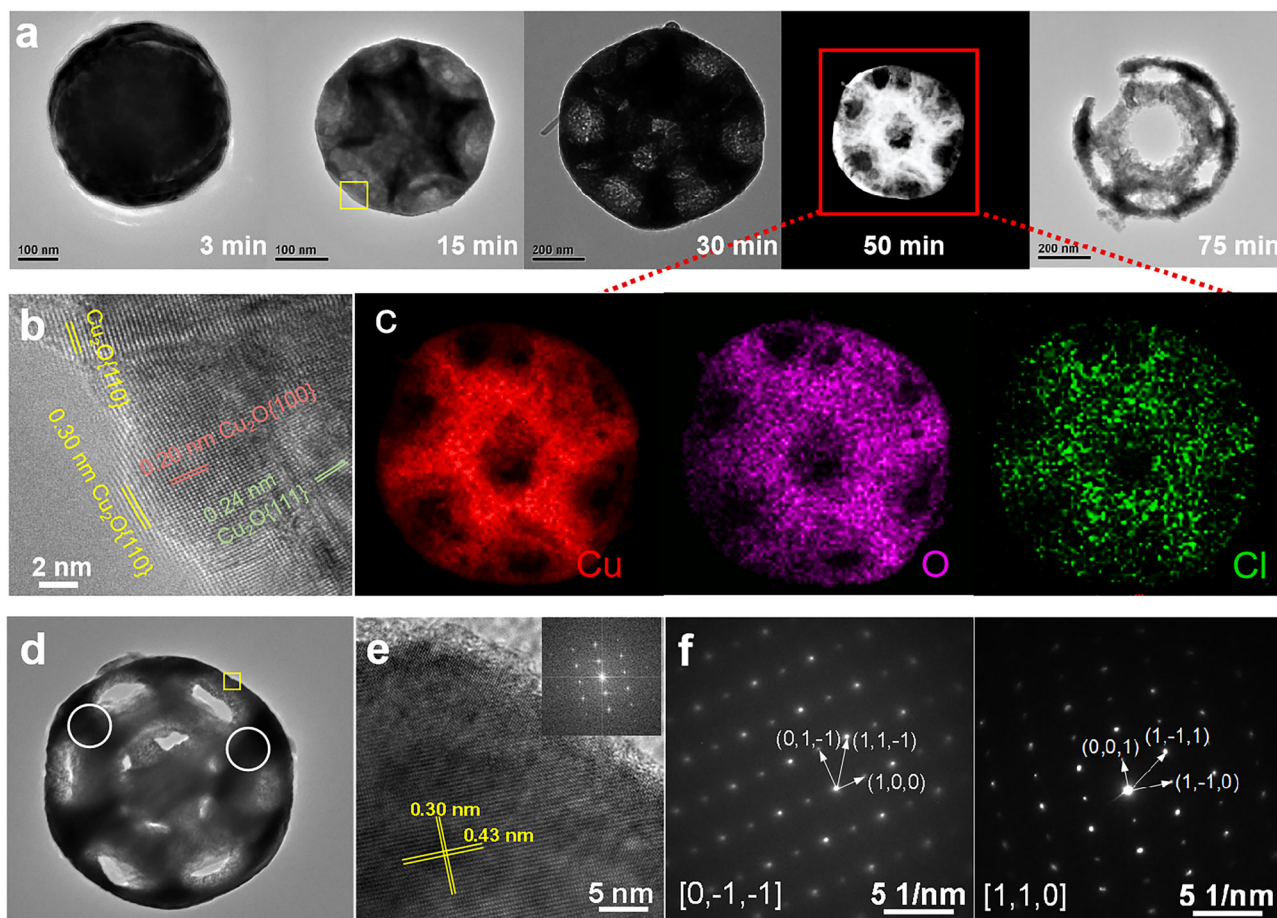

Fig. 3 | Microscopic characterization of s-Cu_2O-NF. a TEM images of the morphology change of s-Cu_2O-NF with different etching times. **b** HRTEM images of the area marked with a yellow rectangle of s-Cu_2O-NF after HCl etching for 15 min. **c** High-angle annular dark-field image of s-Cu_2O-NF and elemental mapping images of Cu, O, and Cl. The (**e**) HRTEM image (inset is the Fast Fourier transform image), (**f**) SAED patterns of the area marked with a yellow rectangle and white circle in (**d**) TEM image of s-Cu_2O-NF.

{110} facets, effectively shielding them from HCl etching. Conversely, the other Cu₂O facets, especially the {111} and {100} facets, were selectively diminished by HCl etching. Utilizing this technique, we have successfully synthesized spherical Cu₂O nanoframes (s-Cu₂O-NF) characterized by an internally hollow structure with the abundance of {110} facets. The as-synthesized s-Cu₂O-NF achieved an impressive selectivity of nearly 100% for propylene oxide (PO) at a relatively low operating temperature of 150 °C, which was superior to that of other Cu₂O nanoparticles in the DEP reaction.

Results

Structure analysis of catalysts

Wet-chemical methods were used to synthesize a number of Cu₂O nanocrystals, which included cubic (c-), octahedral (o-), rhombic dodecahedral (r-), octadecahedral (d-), and spherical (s-) Cu₂O. Furthermore, c-, o-, d- and s-Cu₂O hollow nanoframes (see the experimental section for details) have also been prepared. The scanning electron microscopy (SEM) and transmission electron microscopy (TEM) were used to characterize the morphologies of the synthesized Cu₂O samples. The solid Cu₂O samples were found to possess well-defined cubic, octahedral, rhombic dodecahedral, octadecahedral, and spherical shapes, which were characterized by uniform dispersion and particle size, according to these techniques. The fabricated Cu₂O structures are shown in Fig. 1 and Supplementary Fig. 1 with detailed SEM and TEM images. Among these structures, the spherical Cu₂O (s-Cu₂O) displays a uniformly spherical shape with an average size of ~ 475 nm. The successful preparation of corresponding Cu₂O nanoframes/nanocages with hollow interiors that were clearly distinct from the solid s-Cu₂O nanocrystals was achieved through selective facet etching. Figure 1h demonstrates that the spherical Cu₂O hollow nanocage (s-Cu₂O-NC) assumes a concave, bowl-like form, with a marginally reduced average size. Conversely, the internally hollow Cu₂O nanoframe with spherical shape (s-Cu₂O-NF) (Fig. 1i, j) adopts an intricate, football-like geometry, with a wall thickness estimated at 25–40 nm. Subsequently, the ligand-protection/selective facet-etching strategy was employed to eliminate the {111} and {100} facets from Cu₂O catalysts in order to synthesize spherical Cu₂O nanoframes (s-Cu₂O-NF) (Fig. 1p). This illustration demonstrated that the structure was internally hollow and that there were numerous {110} sites.

XRD was used to confirm the crystal phases of the Cu₂O nanocatalysts that had already been prepared. As shown in Fig. 2a, all the diffraction peaks were well indexed according to a pure phase of Cu₂O (space group: Pn3̄m, lattice constant $a = 0.427$ nm, JCPDS 05-0667[26,27]). The samples did not show any detectable impurities. According to the ligand-protection/selective facet-etching process, s-Cu₂O-NF not only experienced a crystal growth process of up to 2 h, but also existed in an etching stage of up to 50 min for facet-etching and aging process, effectively increasing the intensity of characteristic diffraction peaks. The above two key steps exposed the inner and outer surfaces of s-Cu₂O-NF with the abundance of {110} facets, originating from an internally hollow structure[28]. Notably, these nanoframes showed a significantly increased proportion of {110} facets when compared to the solid Cu₂O nanocrystals. This phenomenon was particularly noticeable in the case of spherical Cu₂O nanoframes, which had a sharp Cu₂O {220} peak. The chemical bonds and inner structures were further analyzed using FT-IR. As depicted in Fig. 2b, it was demonstrated that all Cu₂O nanocatalysts showed the identified peak positions at 628 cm⁻¹ but absent at 550 cm⁻¹. The former could be assigned to the stretching vibrations of Cu(I)−O, while the absence of the latter peak, typically attributed to Cu(II)−O vibrations, further corroborated the predominant presence of Cu₂O in these nanocatalysts[29–31]. Due to the different synthesis methods and the color of the Cu₂O samples (Supplementary Fig. 2), the absorption and transmission of infrared rays were different[32,33]. In addition, as for c-Cu₂O, the intensity of the Cu−O stretching vibration at 628 cm⁻¹ was

also increased due to the contribution of the −CH₂ band at 630 cm⁻¹ in the residual D-glucose[34,35]. In addition, the XPS analysis of C 1s (Supplementary Fig. 3a) revealed only the presence of adventitious carbon species (284.8 eV) and carbonate species (288.4 eV) on the surfaces of spherical Cu₂O nanocatalysts. The XPS analysis of Cu 2p (Fig. 2c) manifested that the surface copper atoms on various spherical Cu₂O were almost the same valence. The in situ DRIFTS (Supplementary Fig. 3b) of CO adsorption discerned vibrational features at 2112, 2125 and 2172 cm⁻¹. Two peaks at 2125 and 2172 cm⁻¹ can be attributed to the gaseous CO[36–39]. Another CO band at 2112 cm⁻¹ can be assigned to the adsorbed CO on Cu(I) sites[11,36,40–42]. After the ligand-protection and selective facet-etching steps, the specific surface area was expanded and the abundance of {110} facets was significantly increased, leading to more pronounced and sharper infrared absorption peaks of CO adsorption.

The morphological transformation of s-Cu₂O-NF during the first two hours of aging, characterized by the predominance of etching processes over crystal growth, has been illustrated in Fig. 3. The spherical Cu₂O sample retained a solid form during the initial phase of HCl-mediated etching, which showed {110} edges with a mixture of other facets internally. A representative high-resolution transmission electron microscopy (HRTEM) image (Fig. 3b), acquired from the region marked with a yellow rectangle, displayed distinct lattice fringes with spacings of 0.21, 0.24 and 0.30 nm, corresponding to the {100}, {111} and {110} facets of Cu₂O, respectively[11,43–45]. It can be observed in Fig. 3d–f, after the appropriate etching time, s-Cu₂O-NF nanocatalysts exhibited a significant exposure of the {110} facets. HRTEM images from regions outlined by a yellow rectangle in Fig. 3d and Supplementary Fig. 4, where the lattice spacings of 0.30 nm and 0.43 nm were identified, demonstrated the typical characteristics of the {110} facets (Supplementary Fig. 5). This was further confirmed by Fast Fourier transform and selected area electron diffraction (SAED). However, the structural degradation and collapse occurred as a result of prolonged etching time. Supplementary Fig. 6 illustrates the connection between crystal phase transformation and morphology of s-Cu₂O-NF during the HCl etching processes. The pure phase of Cu₂O was clearly indicated by the indexing of all the XRD peaks. Due to the adsorption of SDS and its protection for the {111} facet, the XRD peak intensities were low. By using the appropriate facet-etching technique, the inner surface of s-Cu₂O-NF was revealed, with the XRD intensity ratio of {110}/{111} reaching almost 0.28, which is a significant improvement from that in JCPDS 05-0667 (nearly 0.07). Furthermore, the relative peak changes in UV-Vis spectroscopy (Supplementary Fig. 7a) showed similar emission spectra but different intensities over various Cu₂O samples throughout the facet-etching processes. These findings indicated that the source's absorbance changes during the s-Cu₂O-NF facet-etching process within 50 min were responsible for the gradual shift of sample color from yellow to orange-red, which occurred due to the internal hollowing of the structure. The sample color became lighter as the etching time increased, resulting in structural degradation of the s-Cu₂O-NF (Supplementary Fig. 7b)[9,46]. These observations can be explained by three distinct stages in the crystal growth and etching process[24,47]: (1) the reaction of Cu²⁺ and OH⁻ led to Cu(OH)₂ precipitation; (2) the addition of NH₂OH·HCl accelerated the conversion of Cu(OH)₂ precipitates into Cu₂O nanocrystals with trace Cl⁻ incorporating into the crystal lattice[9]; (3) morphology control by the ligand-protection/selective facet-etching strategy confirmed the predominant exposure of the {110} facets.
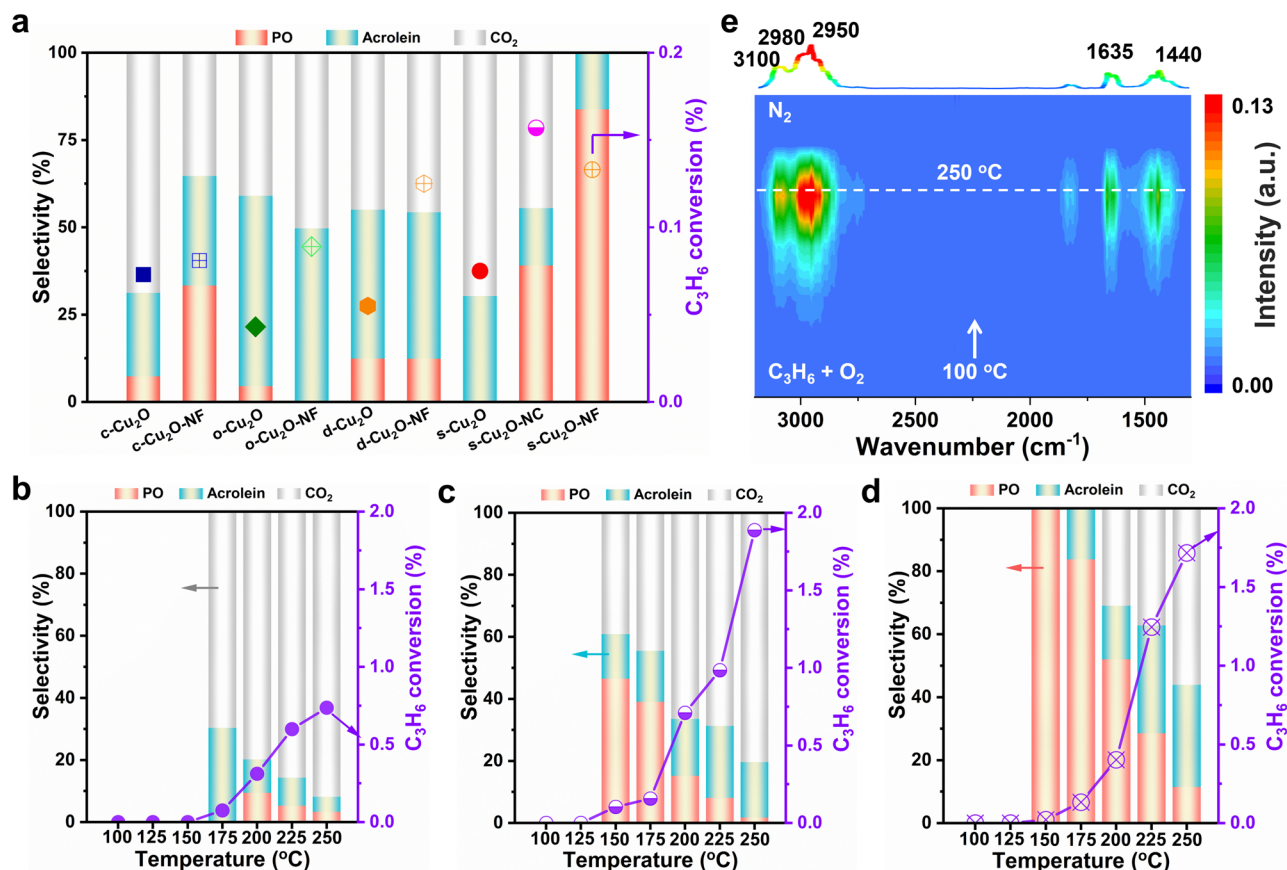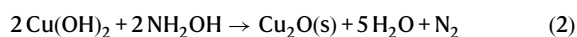
$$2\,Cu^{2+} + OH^{-} \rightarrow Cu(OH)_2(s) \tag{1}$$
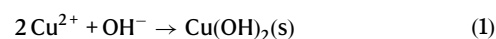
Fig. 4 | Catalytic performance of propylene epoxidation with O_2. Propylene conversion and product selectivity over (**a**) as-prepared Cu_2O nanocatalysts at 175 °C. Propylene conversion and product selectivity over (**b**) s-Cu_2O, (**c**) s-Cu_2O-NC and (**d**) s-Cu_2O-NF at different temperatures. Reaction conditions: C_3H_6: O_2: N_2 = 10: 5: 85 vol.%, GHSV = 36,000 h^{-1}, 50.0 mg catalyst. **e** in situ DRIFTS spectra after exposing s-Cu_2O-NF to the mixed flow of C_3H_6, O_2 and N_2 (10: 5: 85 vol.%).

$$2\,Cu(OH)_2 + 2\,NH_2OH \rightarrow Cu_2O(s) + 5\,H_2O + N_2 \qquad (2)$$

$$Cu_2O(s) + 4\,HCl \rightarrow 2\,HCuCl_2 + H_2O \qquad (3)$$

The EDX mapping analysis can be found in Fig. 3c and Supplementary Fig. 8. The structural integrity of the s-Cu_2O-NF and s-Cu_2O-NC nanomaterials was confirmed by the uniform dispersion of Cu and O elements observed in the comprehensive mapping. The hollow configuration of the engineered Cu_2O nanoframes, as described earlier, was a distinctive feature. A profusion of meso- and macropores was formed as a result of the combined ligand-protection/ selective facet-etching strategy and the inherently porous architecture. Consequently, there was a significant increase in the specific surface area of the internally hollow Cu_2O nanoframes, accompanied by a concomitant increase in pore volume, surpassing that of conventional Cu_2O nanoparticles (Supplementary Fig. 9 and Supplementary Table 1). Specifically, the s-Cu_2O-NF and s-Cu_2O-NC nanomaterials exhibited significantly superior S_{BET} and nitrogen adsorption capacities compared to s-Cu_2O.

DEP with molecular oxygen

The reactivity of Cu_2O nanocatalysts in the DEP reaction was evaluated in a continuous-flow quartz reactor, maintaining a gas mixture composition of $C_3H_6/O_2/N_2 = 10:5:85$ vol.%, pressure (P) of 0.1 MPa, and a flow rate of 30.0 mL min^{-1}. As shown in Supplementary Fig. 10, the facet-controlled selectivity of Cu_2O catalysts can be observed through

the DEP performance comparison of c-, o- and r-Cu_2O nanocrystals, which exposed {100}, {111}, and {110} facets, respectively. The distribution of DEP reaction products demonstrated the critical dependence of PO production on the exposure to the {110} facets. Moreover, the involvement of {100}, {111}, and even higher index facet sites in truncated 26-facet polyhedral Cu_2O catalysts, as visualized in SEM, TEM and simulated structures images in Supplementary Fig. 11, was conducive to the deep oxidation (Supplementary Fig. 12). More importantly, the catalytic performances across various morphologically distinct Cu_2O structures (including c-, o-, d-, and s-Cu_2O) and their hollow counterparts, derived via ligand-protection/selective facet-etching strategy, are shown in Fig. 4 and Supplementary Fig. 13. As expected, the ligand-protection/selective facet-etching strategy was effective and versatile, as evidenced by the enhanced DEP activity originating from the internally hollow Cu_2O structures with predominant Cu_2O{110} facet exposure. Figure 4a demonstrates that the c-Cu_2O-NF and s-Cu_2O-NC/-NF exhibited excellent PO selectivity at 175 °C, and the catalytic performance of the above hollow Cu_2O nanoframes was attributed to the {110} facet or edge-sites that selectively catalyze the propylene epoxidation. Among these, the concurrent presence of hollow structure and exposed {110} facet in s-Cu_2O-NF exhibited the highest PO selectivity of 83.8% at comparable propylene conversions, achieving an optimal PO formation rate of 0.18 mmol g_{cat}^{-1} h^{-1}. A similar trend of DEP performance can be observed at 225 °C (Supplementary Fig. 13). Compared with o-Cu_2O and d-Cu_2O, the smaller XRD intensity ratio of {110}/{111}, with the residual minor {111} and {100} facets on the outer surface of o-Cu_2O-NF and d-Cu_2O-NF, promoted unwanted over-oxidation pathways,

Table 1 | Oxygen compositions of s-Cu₂O, s-Cu₂O-NC and s-Cu₂O-NF

Catalyst	O_α (%)[a]	O_β (%)[a]	O_γ (%)[a]	$O_{\alpha+\beta}$: O_γ[b]
s-Cu₂O	14.1	52.5	33.4	0.57
s-Cu₂O-NC	5.8	33.0	61.2	1.19
s-Cu₂O-NF	12.4	34.1	53.5	2.16

[a]The compositions were determined by O₂-TPD measurement.
[b]The compositions were determined by XPS analysis.

underscoring the necessity of predominantly exposing the {110} active facets (Supplementary Fig. 14).

Interestingly, different spherical Cu₂O samples displayed dramatically different catalytic performances towards the DEP reaction. The PO selectivity (< 10%) was only low for solid Cu₂O nanocrystals (s-Cu₂O) at all reaction temperatures (Fig. 4b), while moderate PO selectivity (40–45%) was attained for hollow Cu₂O nanocages (s-Cu₂O-NC) in the temperature range of 150 °C to 175 °C (Fig. 4c). In comparison, the as-obtained s-Cu₂O-NF, with the predominant exposure of the {110} facets, achieved nearly 100% PO selectivity at 150 °C (Fig. 4d), which can be intriguing and worth considering the separation cost for the products in industry level. When the temperature was elevated to 175 °C, 83.8% PO selectivity was still maintained with the C₃H₆ conversion of 0.14%. Supplementary Fig. 15 displayed the apparent activation energy plots of s-Cu₂O, s-Cu₂O-NC, and s-Cu₂O-NF deduced via the Arrhenius equation. Clearly, the catalysts with higher reactivity had lower apparent activation energies, which indicated that ligand-protection/selective facet-etching treatment not only generated a greater number of active sites but also enhanced intrinsic activity.

It was worth noting that the spherical Cu₂O nanocrystals without etching (s-Cu₂O-3) containing the doped Cl species (as visualized in SEM, high-angle annular dark-field, and elemental mapping images in Supplementary Fig. 16), displayed negligible DEP reactivity and almost no PO selectivity across all reaction temperatures. Furthermore, as shown in Supplementary Figs. 17 and 18, the influence of the controlled variation of Cl supply indicated that unoptimized Cl introduction led to insufficient catalytic activity or structural collapse. The PO selectivity remained the highest only when the internal nanoframe structure was preserved, with predominant exposure of {110} facets. The synergy between Cl and the {110} facets exists but does not overshadow the structural factors, which are the primary determinants of catalytic performance. This emphasizes the irreplaceable role of the ligand-protection/selective facet-etching method. By conducting a comprehensive comparative analysis of the DEP performance (Supplementary Fig. 19 and Supplementary Table 2), s-Cu₂O-NF demonstrated a high PO selectivity and an unprecedented PO formation rate, outperforming those of other coinage-metal-based catalysts.

The in situ DRIFTS measurement of C₃H₆ and O₂ adsorption on s-Cu₂O-NF at different temperatures corroborated the catalytic performance (Fig. 4e). The bands at 1440, 1635, 2950, 2980 and 3100 cm⁻¹ were assigned to CH₂ bending, C = C stretching and a series of methyl symmetrical C − H vibrations arising from propylene adsorption on Cu(I)−O sites. The intensity changes indicated a positive correlation between propylene conversion and reaction temperature[9,11,13]. Stability tests revealed robust catalytic performance of s-Cu₂O-NF at 150 °C, 175 °C and 200 °C over prolonged periods exceeding 300 min. The s-Cu₂O-NF catalyzed the DEP reaction for 300 min with only a slight decrease in the PO selectivity (above 85.2%) and a slight increase of acrolein selectivity at 150 °C (Supplementary Fig. 20a). As depicted in Supplementary Fig. 20b, stability evaluations at 175 °C showed that PO and acrolein were initially predominant products; however, a slight reduction in PO selectivity occurred over time, accompanied by the emergence of CO₂ from deeper oxidation processes. PO remained the

primary product throughout the stability test. In contrast, the active sites on s-Cu₂O-NC and s-Cu₂O exhibited lower stability, with PO selectivity diminishing to negligible levels after the test duration surpassed 100 min (Supplementary Fig. 20e and f). Upon further elevating the reaction temperature to 200 °C, s-Cu₂O-NF maintained stable DEP reactivity and consistent PO selectivity, with PO predominating among reaction products throughout the 300 min testing period (Supplementary Fig. 20c). Post-reaction structural integrity and morphology of the spent s-Cu₂O-NF were confirmed via extensive characterization techniques including XRD, SEM, TEM, HRTEM, and XPS analyses (Supplementary Fig. 21). After the DEP reaction at 150 °C and even up to 200 °C, there were no significant changes in the hollow structure and particle size, indicating that the essential {110} facet sites of s-Cu₂O-NF were still preserved without surface reconstruction. All of these findings accentuated that ligand-protection/selective facet-etching, targeting a larger specific surface area and predominant exposure of Cu₂O {110}, achieves a triple-win: it would not only enhance the activity and selectivity for the DEP reaction, but also strengthen catalyst durability.

Structure sensitivity of Cu₂O catalysts

To obtain in-depth knowledge about the structure sensitivity of distinct Cu₂O nanostructures in the DEP reaction, the EIS, Raman, O₂-TPD, H₂-TPR and XPS analyses were utilized. In the DEP reaction, it was postulated that the chemically adsorbed oxygen species, such as O^- or O_2^-, would preferentially interact with the electron-rich C = C bond of propylene to produce PO, while the nucleophilic lattice oxygen species (O^{2-}) tends to attack the α C − H bond to yield deep-oxidation products[48,49]. It is well established that the chemically adsorbed O₂ will be activated on the catalyst surface along with the charge-transfer phenomenon. Therefore, the surface nature and charge transfer capacity of catalysts have profound implications for the properties of intermediate oxygen species, further determining the pathway of DEP reactions. The Raman analysis was carried out to provide insights into the surface and local chemical structures of the catalysts. Supplementary Fig. 22a revealed that s-Cu₂O-NF had the most obvious crystal defects, which was beneficial to promote electron transfer from the active sites to adsorbed oxygen species based on the strong dependence of transferred electrons on defectiveness. Furthermore, the EIS Nyquist plots provided the internal impedance of s-Cu₂O samples by comparing the radius of the arc, which represented the internal charge transfer resistance: the smaller the radius of the arc, the lower the resistance. As shown in Fig. 5a, s-Cu₂O-NF generated the smallest semicircle radius compared with s-Cu₂O-NC and s-Cu₂O, accompanied by the smallest R_{ct} value (Supplementary Fig. 22b), illustrating that s-Cu₂O-NF possessed the smallest interfacial charge-transfer resistance and the strongest charge transport capacity. Accordingly, the Raman and EIS results were employed to characterize the charge-transfer properties of the reactive oxygen species on s-Cu₂O and its derivatives. Collectively, these results suggest that s-Cu₂O-NF offers superior electron and molecule transfer kinetics, enhancing the electron transfer from the surface to molecular O₂ to generate O^- or O_2^- on the surface[50–52].

In addition, O₂-TPD was conducted to gain insights into the oxygen species. Typically, three types of oxygen species can be identified on the Cu₂O surface, namely surface adsorbed oxygen (O_α), chemically adsorbed oxygen (O_β, O^- or O_2^-), and lattice oxygen (O_γ). As shown in Fig. 5b, only weak desorption peaks, primarily at the lattice oxygen desorption temperatures, were observed on the s-Cu₂O, indicating that nearly no adsorbed oxygen species were involved. In contrast, s-Cu₂O-NF exhibited three distinct desorption peaks located at 243, 331, and 404 °C. However, for s-Cu₂O-NC, the weaker O_α intensity but stronger O_γ intensity was observed at higher temperatures (361 and 432 °C, respectively). Combined with the data split graph of O₂-TPD (Supplementary Fig. 23) and the relative contents (Table 1), it could be
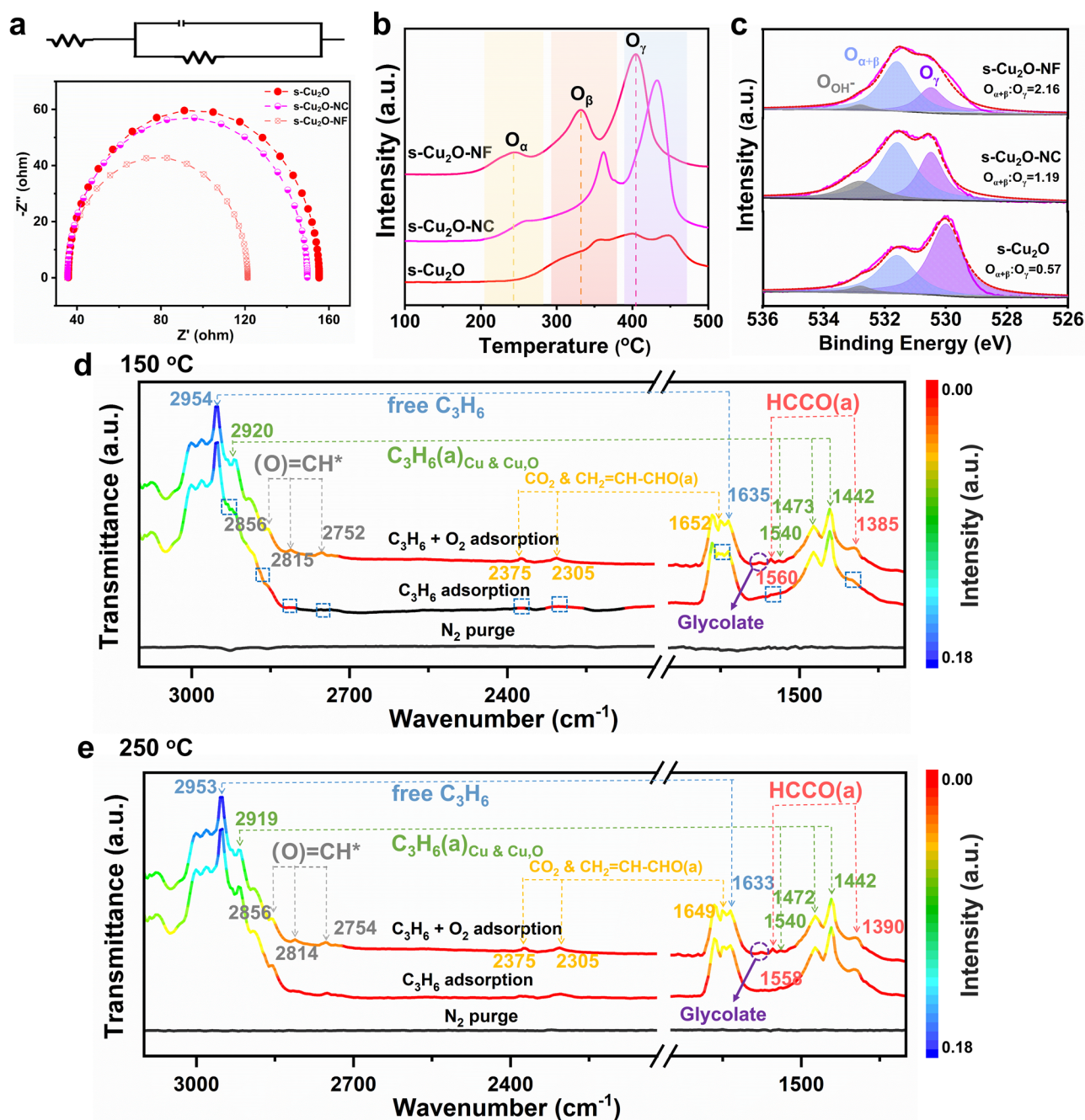
Fig. 5 | Structure sensitivity of Cu₂O catalysts and DEP process studies. (a) EIS spectra (using a 1 M KOH electrolyte dissolved in deionized water), **(b)** O₂-TPD patterns and **(c)** XPS patterns of O of s-Cu₂O, s-Cu₂O-NC and s-Cu₂O-NF. In situ DRIFTS spectra after exposing s-Cu₂O-NF to the flow of C_3H_6 and mixed flow of C_3H_6, O_2 and N_2 (10: 5: 85 vol.%) at **(d)** 150 °C and **(e)** 250 °C.

inferred that the excellent PO selectivity via s-Cu₂O-NF might be attributed to the abundant O^- or O_2^- species thereon. XPS measurements were further undertaken to investigate the surface oxygen species of the Cu₂O samples. The O 1s spectra presented asymmetric peaks, indicating that the presence of different oxygen species on Cu₂O catalysts can be identified as hydroxyl (O_{OH^-}, 532.8 eV), surface adsorbed oxygen ($O_{\alpha+\beta}$, 531.5 eV), and lattice oxygen (O_β, 530.0-530.5 eV), respectively[53,54]. Furthermore, the $O_{\alpha+\beta}$ peak of s-Cu₂O-NF and s-Cu₂O-NC shifted to a higher binding energy than that of s-Cu₂O, attributed to the electron transfer from the Cu₂O surface to O_2. The ratio of the oxygen species has been summarized in Table 1. Impressively, s-Cu₂O-NF, synthesized through the ligand-protection/selective facet-etching strategy, exhibited a higher proportion of chemically

adsorbed oxygen species (O^- or O_2^-). The H₂-TPR experiments (Supplementary Fig. 24) were also carried out to identify the surface oxygen species below 400 °C. The results revealed that the reduction peak of s-Cu₂O-NF shifted to a lower temperature compared to s-Cu₂O-NC, implying greater H₂ consumption. Thus, the conclusion could be drawn that, in contrast to s-Cu₂O and s-Cu₂O-NC, s-Cu₂O-NF harbors a higher proportion of chemically adsorbed oxygen species that can promote PO formation.

Catalytic mechanism studies

In situ DRIFTS was also utilized to investigate the oxidative process of propylene with O_2 over s-Cu₂O-NF catalysts. The experiments were conducted under conditions introducing C_3H_6 and $C_3H_6 + O_2$ in the
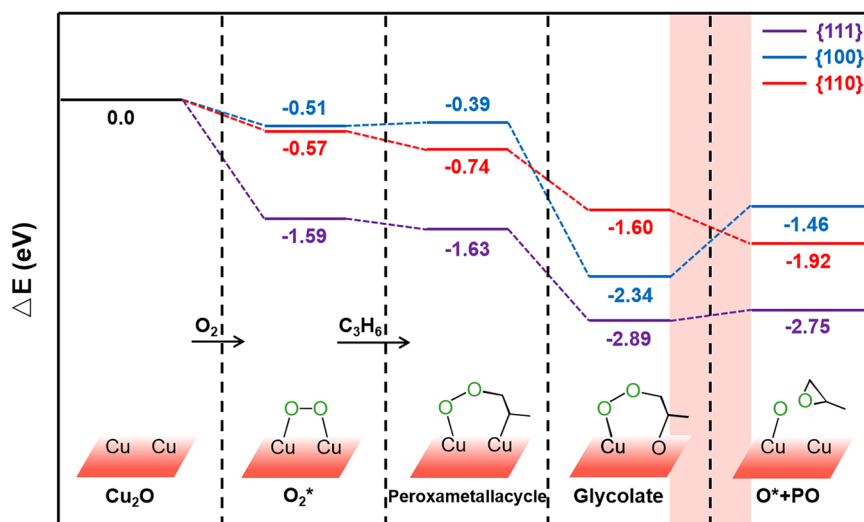
Fig. 6 | DFT calculations. The relative energies of oxygen species and possible intermediates for the reaction of propylene with O_2^* over Cu_2O {111}, {100}, and {110} surfaces, respectively.

range of 150 °C to 250 °C (0.1 MPa). After N_2 purging thoroughly, s-Cu_2O-NF was exposed to a C_3H_6 flow or $C_3H_6 + O_2$ mixed flow, resulting in the appearance of various IR features (Fig. 5d, e and Supplementary Fig. 25). The assignments of these vibrational features have been summarized in Supplementary Table S3. Among them, the bands at 1635 and 2954 cm^{-1} were indicative of the C = C and CH_3 stretching vibrations, respectively, representing a free C_3H_6 molecule. Concurrently, the peaks proximate to 1440, 1473, 1540, and 2920 cm^{-1} were ascribed to C_3H_6 adsorbed at Cu(I) sites or bridging Cu–O sites of Cu_2O {110} (noted as $C_3H_6(a)_{Cu \& Cu,O}$)[11,13]. Significantly, the vibrational features of intermediates during the DEP reaction process exhibited distinct variations when a mixed flow of C_3H_6 and O_2 was introduced as compared to the C_3H_6 flow at 150 °C. The appearance of IR bands at 2752, 2815, and 2856 cm^{-1} arising from C − H stretching, which were split by Fermi resonance, emerged exclusively in the mixture of $C_3H_6 + O_2$, signifying intermediates involved in PO production. Interestingly, the same vibrational bands could be observed via PO adsorption (Supplementary Fig. 26)[10,49]. In addition, characteristic IR peaks associated with intermediates for acrolein or CO_2 production, including HCOO(a) (1385 and 1560 cm^{-1}), $C_3H_4O(a)$ (1652 cm^{-1}), and CO_2 (manifesting as a pair of weak IR bands at 2305 and 2375 cm^{-1}), were observed in the presence of $C_3H_6 + O_2$ but were absent with C_3H_6 flow[11,49,55,56]. These results suggested that the reaction process occurred only when the catalyst was exposed to an external source O_2 at 150 °C. A similar phenomenon can be observed at a reaction temperature of 175 °C, at which the PO formation rate became most optimistic. With further heating, the aforementioned vibrational features were similar upon chemisorption of $C_3H_6 + O_2$ mixed flow or C_3H_6 flow on s-Cu_2O-NF (Supplementary Fig. 27). Based on the in situ FT-IR spectra of propylene epoxidation, it can be concluded that the DEP reaction catalyzed by s-Cu_2O-NF would follow the Langmuir-Hinshelwood (LH) mechanism at a relatively low operational temperature, utilizing surface-adsorbed oxygen rather than lattice oxygen to interact with C_3H_6. In contrast, above 175 °C, the Mars-van Krevelen (MvK) mechanism used lattice oxygen as the active oxygen species. It preferentially attacked the α C−H bond of propylene and gradually took the initiative in the DEP reaction. Until reaching 250 °C, as shown in Fig. 5e, the vibrational features of C_3H_6 chemisorption were similar to those of $C_3H_6 + O_2$, except that their intensities were reduced. These DRIFTS results presented that s-Cu_2O-NF catalyzed the DEP reaction following the MvK mechanism, and this trend became fully visible, resulting in deep oxidation.

Computational studies

To elucidate the influence of different morphologies of Cu_2O on the DEP reaction, we employed periodic density functional theory (DFT) calculations to assess the adsorption characteristics of Cu_2O {111}, Cu_2O {100} and Cu_2O {110} (Fig. 6 and Supplementary Table 4).

Initially, we examined the adsorption of molecular oxygen (O_2^*, indicating chemically adsorbed oxygen) and the epoxidation product (O* + PO). The DFT results revealed that O_2^* exhibited strong adsorption on the Cu_2O {111} surface with an adsorption energy of − 1.74 eV, in contrast to the relatively weak adsorption on Cu_2O {100} and Cu_2O {110} surfaces, which presented adsorption energies of − 0.51 eV and − 0.57 eV, respectively. Analysis of Bader charges indicated that the adsorbed O_2^* on these surfaces acquired negative charges of 0.58 |e|, 0.10 |e|, and 0.27 |e|, respectively, suggesting the formation of superoxide species. Concerning the epoxidation product, the Cu_2O {111} surface demonstrated the most substantial adsorption energy (− 2.89 eV), followed by the Cu_2O {110} (− 1.92 eV) and Cu_2O {100} (− 1.46 eV) surfaces. These results, however, could not explain why only the Cu_2O {110} exhibits excellent DEP performance.

Accordingly, we shifted our attention to the adsorption of possible epoxidation intermediates. As depicted in Fig. 6, the interaction among the propylene C = C bond, the adsorbed O_2^*, and an adjacent Cu atom can lead to the formation of peroxametallacycle species, which was usually postulated as a critical intermediate in the epoxidation process[57–59]. DFT calculations demonstrated that these peroxametallacycle species exhibited only marginal adsorption energies, ranging from + 0.12 to − 0.17 eV relative to $O_2^* + C_3H_6$, thereby downplaying their significance in DEP. Alternatively, the interaction among the propylene C = C bond, the adsorbed O_2^*, and a nearby oxygen atom (rather than Cu atom) can result in relatively stable glycolate intermediates, with adsorption energies ranging from − 1.02 to − 1.95 eV with respect to $O_2^* + C_3H_6$. In principle, these glycolate intermediates are expected to be more stable than the PO intermediates due to the lower strain in the former case. Intriguingly, our findings suggested that PO would be the most stable species on the Cu_2O {110} surface, while glycolate intermediates exhibited the highest stability on both Cu_2O {111} and Cu_2O {110} surfaces. This phenomenon arose from the unique atomic arrangement of copper and oxygen on the {110} facet, which provided a confined environment conducive to the formation of a distorted adsorption structure for the glycolate intermediate. This assertion was substantiated by the elongation of the C-O_{surf} bond length on Cu_2O {110} as compared to Cu_2O {111} and Cu_2O

{100}, as detailed in Supplementary Table S3. Notably, as shown in Fig. 5d, e and Supplementary Fig. 27, the IR features belonging to glycolate intermediates, such as C−O stretching (1180–1210 cm^{-1}), and the IR band located at 1578 cm^{-1} which was ascribed to the formation of glycolate[60–62] can be observed upon adsorption of $C_3H_6 + O_2$ mixed flow at both 150 °C and 250 °C. Consequently, these findings came to the conclusion that PO would be predominantly generated on the Cu_2O {110} surface during the DEP, while by-products would be more prevalent on the Cu_2O {111} and Cu_2O {110}, nicely accounting for the experimental observations.

To summarize, we have successfully employed a ligand-protection/selective facet-etching strategy to synthesize internally hollow Cu_2O nanoframes, amplifying the exposure of {110} facets. Our work highlights the distinct advantages of Cu_2O {110} in generating chemically adsorbed oxygen species (O$^-$ or O$_2^-$), which in turn markedly improved DEP reactivity, PO selectivity and catalyst stability, realizing a triple-win. Impressively, s-Cu_2O-NF achieved > 99% PO selectivity at 150 °C, outperforming any other Cu_2O nanocatalysts previously reported. Through comprehensive characterizations, we proposed that at relatively low temperatures, the DEP reaction occurred through the LH mechanism with adsorbed O_2 species acting as the oxidant. Furthermore, DFT calculations have elucidated that PO became the dominant product only when it was thermodynamically more favorable compared to other intermediates for the reaction of propylene and O_2^*.

Methods

Materials

Copper chloride dihydrate ($CuCl_2·2H_2O$), sodium hydroxide (NaOH), hydroxylamine hydrochloride ($NH_2OH·HCl$), oleic acid (OA), glucose, L-ascorbic acid (AA), lauryl sodium sulfate (SDS), ethanol, cyclohexane and hydrochloric acid (HCl) were purchased from Sinopharm Chemical Reagent Co., Ltd. Copper sulfate pentahydrate ($CuSO_4·5H_2O$) was purchased from Macklin Reagent company. Sodium potassium tartrate tetrahydrate (SPTT), potassium hydroxide (KOH), palladium chloride ($PdCl_2$) and copper acetate monohydrate (($CH_3COO)_2Cu·H_2O$) were purchased from Aladdin Biochemical Technology Co., Ltd. Polyvinylpyrrolidone (PVP) was purchased from Beijing Wokai Biotechnology Co., Ltd. All chemical reagents were used as received without further purification. All aqueous solutions were prepared using deionized water with a resistivity of 18.2 MΩ cm^{-1}.

Synthesis of spherical Cu_2O nanocrystals (s-Cu_2O)

s-Cu_2O was synthesized according to the method improved by the reported study of Zhan et al.[9] 0.073 g $Cu(NO_3)_2·3H_2O$ and 0.60 g PVP were dissolved in 35.0 mL deionized water with constant stir. Then, 6.0 mL NaOH solution (0.20 mol L^{-1}) was added dropwise to the above solution (~195 s) and continued to stir for 10 min. After that, a fresh ascorbic solution (0.10 mol L^{-1}) was added dropwise within 10.5 min, and the mixture was adequately stirred for another 10 min. The original product was washed with ethanol for several times, and dried under vacuum at 60 °C overnight.

Synthesis of spherical Cu_2O nanocages (s-Cu_2O-NC)

s-Cu_2O-NC was synthesized according to the method reported by Yu et al.[63]. The experimental steps are as follows: 1.40 g ($CH_3COO)_2Cu·H_2O$ was accurately weighed and dissolved in 35.0 mL deionized water. The above precursor solution was poured into a 50.0 mL steel autoclave coated with Teflon. Subsequently, the steel autoclave reactor was placed in an oven for 24 h at 200 °C. The resulting mixture was collected by centrifugation and thoroughly washed with deionized water and ethanol. The brick-red product was dried under vacuum at room temperature overnight.

Synthesis of spherical Cu_2O nanoframes (s-Cu_2O-NF)

Typically, 91.1 mL deionized water, 1.0 mL $CuCl_2$ (0.1 mol L^{-1}) and 0.87 g SDS were successively added into a conical flask. The conical flask was placed in a 33 °C oil bath with stirring for the complete dissolution of SDS powder. After that, 5.0 mL NaOH solution (5.0 mol L^{-1}) was added, and it formed a blue precipitate of $Cu(OH)_2$ immediately, along with the solution color changing blue. Next, 4.5 mL of $NH_2OH·HCl$ (2.0 mol L^{-1}) was quickly injected, and the solution was stirred for 20 s until the color of the solution changed from light blue to green. After aging for 2 h, 9.0 mL HCl solution (2.0 mol L^{-1}) was introduced with stirring for another 20 s, and the solution color changed from green to yellow. After etching for 50 min, the obtained product was washed with ethanol and deionized water for several times and dried under vacuum at 70 °C for 12 h.

Characterization methods

The crystalline structure identification of the Cu_2O catalysts was analyzed by X-ray diffraction (XRD, Rigaku Ultima IV) with Cu K$_\alpha$ radiation (λ = 1.54 Å), which operated at a voltage of 35 kV and a current of 15 mA with a step size of 0.02°. The N_2 adsorption isotherms were obtained using an automatic physical adsorber (ASAP2460, Micromeritics) at −196 °C and the surface area was determined by the Brunauer-Emmett-Teller (BET) model. X-ray photoelectron spectroscopy (XPS, Scientific K-Alpha, Thermo Fisher) analysis was carried out to obtain the surface properties of samples under a tube voltage of 15 kV and current of 10 mA. The morphologies, sizes and crystallographic features of the Cu_2O catalysts were characterized by scanning electron microscopy (SEM, Zeiss, Sigma) and transmission electron microscopy (TEM, Philips, TECNAI F30) with energy-dispersive X-ray spectroscopy (EDX) and a double-tilt sample holder. The Fourier transform-infrared spectroscopy (FT-IR) of Cu_2O catalysts were obtained by a Nicolet 6700 FT-IR spectrometer in the frequency range 3500–600 cm^{-1}. Diffuse reflectance infrared Fourier transform spectroscopy (DRIFTS) was measured on a Nicolet 6700 FT-IR spectrometer equipped with an in situ Fourier transform infrared reaction cell and a liquid nitrogen cooled mercury-cadmium-telluride detector. The Raman spectra of representative catalysts were measured at room temperature employing an instrument with a microscope attachment (Thermo Fischer DXR 2Xi). Local structures were determined by Raman spectroscopy (DXR 2Xi, Thermo Fisher) using a 532 nm excitation source. Electrochemical impedance spectroscopy (EIS) measurements were based on a Biologic VMP3 electrochemical workstation. H_2 temperature-programmed reduction (H_2-TPR) experiments were conducted using a chemisorption analyzer equipped with a thermal conductivity detector (Baidewo Instruments, MFTP-3060).

O_2 temperature-programmed desorption (O_2-TPD) characterization

O_2-TPD experiments were carried out in a Micromeritics Autochem II ASAP 2920 apparatus was used for O_2-TPD experiments that involved recording the signal and determining the oxygen species and their corresponding concentrations on the catalyst surface with a TCD (Baidewo Instruments, MFTP-3060). Typically, the nanocatalyst sample (50.0 mg) was purged for an hour at 150 °C with argon flow (30 mL min^{-1}). After cooling down to room temperature, it was saturated with 5% O_2/Ar flow (30 mL min^{-1}) at 50 °C for 2 h. After the above steps, the nanocatalyst sample was heated from room temperature to 520 °C with helium at a heating rate of 5 °C min^{-1}.

Catalytic performance evaluation

The DEP catalytic performance of synthesized Cu_2O catalysts was monitored in a continuous flow fixed-bed microreactor at atmospheric pressure with an axial quartz sheathed thermocouple. Typically, a 50.0 mg Cu_2O sample was equipped in a quartz reactor. The reactant gas mixture (C_3H_6: O_2: N_2 = 10: 5: 85 vol.%) with a flow rate of

30 mL min^{-1} was fed into the reactor to start the reaction, and the reaction temperature was increased from 125 °C to 275 °C at a rate of 5 °C min^{-1}. The lines and valves of the reactor and the gas chromatographs were heated to 110 °C, preventing the condensation of products[64,65]. The reactants and product were analyzed via two gas chromatographs (GC) equipped with three columns in real time. The outlet CO_2, C_3H_6, and O_2 were analyzed by a thermal conductivity detector (TCD, separated by a Porapak column and a molecular sieve 5 A column). The outlet propylene oxide (PO), acrolein, acetone, propionaldehyde, isopropanol and acetaldehyde products were detected by a flame ionization detector (FID, separated by a capillary column). Considering the difference in carbon number of different products, the catalytic activity, selectivity of PO and its formation rate were calculated as the following equations:

$$X_i = R_i \times A_i \qquad (4)$$

$$\sum X_i = \sum X_{Products, C3} + \sum \frac{2X_{Products, C2}}{3} + \sum \frac{X_{Products, C1}}{3} \qquad (5)$$

$$C_{C3H6} = \sum \frac{X_i}{X_{C3H6, infeed}} \times 100\% \qquad (6)$$

$$S_i = \frac{N_i}{3} \times \frac{X_i}{\sum X_i} \times 100\% \qquad (7)$$

$$PO\,\text{formation rate} = \frac{C_{C3H6} \times F_{C3H6} \times Pressure \times S_{PO}}{R \times T \times m} \qquad (8)$$

Where X_i represents the concentration of reactants or products, A_i represents conversion of the peak area obtained by GC, R_i is the relative correction factor resulting from the standard gases, C_{C3H6} represents C_3H_6 conversion, $X_{C3H6,infeed}$ represents the concentrations of C_3H_6 at the inlet, N_i represents the carbon number in each product, S_i represents the selectivity of various products. F_{C3H6} represents the flow rate of C_3H_6, m_{cat} represents the mass of the catalyst.

Data availability
Data will be made available on request. Source data are provided in this paper.

References

1. Teržan, J., Huš, M., Likozar, B. & Djinović, P. Propylene epoxidation using molecular oxygen over copper- and silver-based catalysts: A review. *ACS Catal.* **10**, 13415–13436 (2020).
2. Du, M. et al. Ionic liquid-enhanced immobilization of biosynthesized Au nanoparticles on TS-1 toward efficient catalysts for propylene epoxidation. *J. Catal.* **283**, 192–201 (2011).
3. Lin, M., Xia, C., Zhu, B., Li, H. & Shu, X. Green and efficient epoxidation of propylene with hydrogen peroxide (HPPO process) catalyzed by hollow TS-1 zeolite: A 1.0 kt/a pilot-scale study. *Chem. Eng. J.* **295**, 370–375 (2016).
4. Wu, J., Wu, Y. & Wang, J. Comparative study on corrosion behavior of Cu and Sn under UV light illumination in chloride-containing borate buffer solution. *Corros. Sci.* **186**, 109471 (2021).
5. Nijhuis, T. A., Makkee, M., Moulijn, J. A. & Weckhuysen, B. M. The production of propene oxide: Catalytic processes and recent developments. *Ind. Eng. Chem. Res.* **45**, 3447–3459 (2006).
6. Kube, P. et al. Green synthesis of propylene oxide directly from propane. *Nat. Commun.* **13**, 7504 (2022).
7. Wang, L. et al. Titanium silicalite-1 zeolite encapsulating Au particles as a catalyst for vapor phase propylene epoxidation with H_2/O_2: a matter of Au–Ti synergic interaction. *J. Mater. Chem. A* **8**, 4428–4436 (2020).
8. Khatib, S. J. & Oyama, S. T. Direct oxidation of propylene to propylene oxide with molecular oxygen: A review. *Catal. Rev.* **57**, 306–344 (2015).
9. Zhan, C. et al. Critical roles of doping Cl on Cu_2O nanocrystals for direct epoxidation of propylene by molecular oxygen. *J. Am. Chem. Soc.* **142**, 14134–14141 (2020).
10. Li, W. et al. Direct propylene epoxidation with molecular oxygen over cobalt-containing zeolites. *J. Am. Chem. Soc.* **144**, 4260–4268 (2022).
11. Hua, Q. et al. Crystal-plane-controlled selectivity of Cu_2O catalysts in propylene oxidation with molecular oxygen. *Angew. Chem. Int. Ed.* **126**, 4956–4961 (2014).
12. Nguyen, V. et al. Direct gas-phase photocatalytic epoxidation of propylene with molecular oxygen by photocatalysts. *Chem. Eng. J.* **179**, 285–294 (2012).
13. Xiong, W. et al. Fine cubic Cu_2O nanocrystals as highly selective catalyst for propylene epoxidation with molecular oxygen. *Nat. Commun.* **12**, 5921 (2021).
14. Song, Y. & Wang, G. Theoretical study of propylene epoxidation over $Cu_2O(111)$ surface: Activity of O^{2-}, O^-, and O_2^- species. *J. Phys. Chem. C* **122**, 21500–21513 (2018).
15. Wang, Q., Zhan, C., Zhou, L., Fu, G. & Xie, Z. Effects of Cl^- on Cu_2O nanocubes for direct epoxidation of propylene by molecular oxygen. *Catal. Commun.* **135**, 105897 (2020).
16. Torquato, L. D. M. et al. Relation between the nature of the surface facets and the reactivity of Cu_2O nanostructures anchored on $TiO_2NT@PDA$ electrodes in the photoelectrocatalytic conversion of CO_2 to methanol. *Appl. Catal. B Environ. Energy* **261**, 118221 (2020).
17. Li, Y. et al. Effective periodate activation by peculiar Cu_2O nanocrystal for antibiotics degradation: The critical role of structure and underlying mechanism study. *Appl. Catal. B Environ. Energy* **341**, 123351 (2024).
18. An, Y. et al. Hollow structured copper-loaded self-floating catalyst in sulfite-induced oxidation of arsenic(III) at neutral pH: Kinetics and mechanisms investigation. *Chem. Eng. J.* **407**, 127193 (2021).
19. Dong, Y., Jiang, X., Mo, J., Zhou, Y. & Zhou, J. Hollow CuO nanoparticles in carbon microspheres prepared from cellulose-cuprammonium solution as anode materials for Li-ion batteries. *Chem. Eng. J.* **381**, 122614 (2020).
20. Sui, Y. et al. Synthesis of Cu_2O nanoframes and nanocages by selective oxidative etching at room temperature. *Angew. Chem. Int. Ed.* **49**, 4282–4285 (2010).
21. Shang, Y. et al. A facile top-down etching to create a Cu_2O jagged polyhedron covered with numerous 110 edges and 111 corners with enhanced photocatalytic activity. *Chem. Eur. J.* **18**, 14261–14266 (2012).
22. Tang, L. et al. One-pot synthesis of etched Cu_2O cubes with exposed {110} facets with enhanced visible-light-driven photocatalytic activity. *Phys. Chem. Chem. Phys.* **17**, 29479–29482 (2015).
23. Tsai, Y. et al. Fabrication of diverse Cu_2O nanoframes through face-selective etching. *J. Phys. Chem. C* **117**, 24611–24617 (2013).
24. Kuo, C. & Huang, M. Facile synthesis of Cu_2O nanocrystals with systematic shape evolution from cubic to octahedral structures. *J. Phys. Chem. C* **112**, 18355–18360 (2008).
25. Qin, C., Campbell, B. M., Shen, M., Zhao, T. & Sadtler, B. Light-driven, facet-selective transformation of cuprous oxide microcrystals to hollow copper nanoshells. *Chem. Mater.* **31**, 8000–8011 (2019).
26. Wang, W. et al. A photo catalyst of cuprous oxide anchored MXene nanosheet for dramatic enhancement of synergistic antibacterial ability. *Chem. Eng. J.* **386**, 124116 (2020).
27. Subhan, F. et al. Ammonia assisted functionalization of cuprous oxide within confined spaces of SBA-15 for adsorptive desulfurization. *Chem. Eng. J.* **339**, 557–565 (2018).

28. Zhang, Y., Deng, B., Zhang, T., Gao, D. & Xu, A.-W. Shape effects of Cu_2O polyhedral microcrystals on photocatalytic activity. *J. Phys. Chem. C* **114**, 5073–5079 (2010).

29. Bhaisare, M. L., Khan, M. S., Pandey, S., Gedda, G. & Wu, H.-F. Shape-oriented photodynamic therapy of cuprous oxide (Cu_2O) nanocrystals for cancer treatment. *RSC Adv.* **7**, 23607–23614 (2017).

30. Guo, Y. et al. Fabrication of Ag–Cu_2O/reduced graphene oxide nanocomposites as surface-enhanced raman scattering substrates for in situ monitoring of peroxidase-like catalytic reaction and biosensing. *ACS Appl. Mater. Interfaces* **9**, 19074–19081 (2017).

31. Wei, B., Yang, N., Pang, F. & Ge, J. Cu_2O–CuO hollow nanospheres as a heterogeneous catalyst for synergetic oxidation of CO. *J. Phys. Chem. C* **122**, 19524–19531 (2018).

32. Al-Saeedi, S. I., Al-Senani, G. M., Abd-Elkader, O. H. & Deraz, N. M. One pot synthesis, surface and magnetic properties of Cu_2O/Cu and Cu_2O/CuO Nanocomposites. *Crystals* **11**, 751 (2021).

33. Wang, W. et al. Properties analysis of self-luminous cement-based materials with different colors and their visual comfort evaluation on pavement. *Sol. Energy* **247**, 214–227 (2022).

34. Shoeib, M. A., Abdelsalam, O. E., Khafagi, M. G. & Hammam, R. E. Synthesis of Cu_2O nanocrystallites and their adsorption and photocatalysis behavior. *Adv. Powder Technol.* **23**, 298–304 (2012).

35. Ahmed, A., Gajbhiye, N. S. & Joshi, A. G. Low cost, surfactant-less, one pot synthesis of Cu_2O nano-octahedra at room temperature. *J. Solid State Chem.* **184**, 2209–2214 (2011).

36. Teng, Z. et al. CO self-sustained catalytic combustion over morphological inverse model CeO_2/Cu_2O catalysts exposing (1 0 0), (1 1 1) and (1 1 0) planes. *Appl. Catal. B Environ. Energy* **339**, 123119 (2023).

37. Zou, W. et al. Crystal-plane effects on surface and catalytic properties of Cu_2O nanocrystals for NO reduction by CO. *Appl. Catal. Gen.* **505**, 334–343 (2015).

38. Bera, P., Cámara, A. L., Hornés, A. & Martínez-Arias, A. Comparative in situ DRIFTS-MS study of ^{12}CO- and ^{13}CO-TPR on CuO/CeO_2 catalyst. *J. Phys. Chem. C* **113**, 10689–10695 (2009).

39. Hornés, A. et al. CO-TPR-DRIFTS-MS in situ study of CuO/$Ce_{1-x}Tb_xO_{2-y}$ (x = 0, 0.2 and 0.5) catalysts: Support effects on redox properties and CO oxidation catalysis. *J. Catal.* **268**, 367–375 (2009).

40. Yang, T. et al. Coordination tailoring of Cu single sites on C_3N_4 realizes selective CO_2 hydrogenation at low temperature. *Nat. Commun.* **12**, 6022 (2021).

41. Zuo, H. et al. Hydrogen production and CO_2 capture from Linz-Donawitz converter gas via a chemical looping concept. *Chem. Eng. J.* **477**, 146870 (2023).

42. Zhang, Z. et al. Structure sensitivity of CuO in CO oxidation over CeO_2-CuO/Cu_2O catalysts. *J. Catal.* **405**, 333–345 (2022).

43. Zhang, S. et al. Sub-3 nm ultrafine Cu_2O for visible light driven nitrogen fixation. *Angew. Chem. Int. Ed.* **60**, 2554–2560 (2021).

44. Ye, Y. et al. Cell wall destruction and internal cascade synergistic antifungal strategy for fungal keratitis. *ACS Nano* **16**, 18729–18745 (2022).

45. Yao, S. et al. Anchoring ultrafine Cu_2O nanocluster on PCN for CO_2 photoreduction in water vapor with much improved stability. *Appl. Catal. B Environ. Energy* **317**, 121702 (2022).

46. Xiao, M. et al. Quasi-single crystalline cuprous oxide wafers via stress-assisted thermal oxidation for optoelectronic devices. *Adv. Funct. Mater.* **32**, 2110505 (2022).

47. Lv, T.-T. et al. Protection of highly active sites on Cu_2O nanocages: an efficient crystalline catalyst for ammonium perchlorate decomposition. *CrystEngComm* **22**, 8214–8220 (2020).

48. Wang, Y., Chu, H., Zhu, W. & Zhang, Q. Copper-based efficient catalysts for propylene epoxidation by molecular oxygen. *Catal. Today* **131**, 496–504 (2008).

49. Wang, Y., Ma, W., Wang, D. & Zhong, Q. Study on the reaction mechanism of the propylene oxide rearrangement via in situ DRIFTS. *Chem. Eng. J.* **307**, 1047–1054 (2017).

50. Hu, Y., Wan, X., Tie, S., Lan, S. & Gao, X. Synthesis of a new porous $Cu_2O@Cu_4(SO_4)(OH)_6\cdot2H_2O$ core-shell thermocatalyst by in situ etching for efficient catalytic degradation of dye under dark condition. *J. Solid State Chem.* **298**, 122107 (2021).

51. Xu, Y. et al. Ultralow-content Pd in-situ incorporation mediated hierarchical defects in corner-etched Cu_2O octahedra for enhanced electrocatalytic nitrate reduction to ammonia. *Appl. Catal. B Environ. Energy* **306**, 121094 (2022).

52. Huo, H. et al. Solar-driven CO_2-to-ethanol conversion enabled by continuous CO_2 transport via a superhydrophobic Cu_2O nano fence. *Chem. Sci.* **15**, 1638–1647 (2024).

53. Zhu, Y. et al. Regulating CeO_2 morphologies on the catalytic oxidation of toluene at lower temperature: A study of the structure–activity relationship. *J. Catal.* **418**, 151–162 (2023).

54. Wang, Y. et al. Metal support interaction of defective-rich CuO and Au with enhanced CO low-temperature catalytic oxidation and moisture resistance. *Adv. Powder Mater.* **2**, 100119 (2023).

55. Chen, S. et al. Probing surface structures of CeO_2, TiO_2, and Cu_2O nanocrystals with CO and CO_2 Chemisorption. *J. Phys. Chem. C* **120**, 21472–21485 (2016).

56. Liang, M., Zhu, X. & Ma, W. The propylene oxide rearrangement catalyzed by the lewis acid sites of ZSM-5 catalyst with controllable surface acidity. *Catal. Lett.* **149**, 942–949 (2019).

57. Yang, H., Li, G., Jiang, G., Zhang, Z. & Hao, Z. Heterogeneous selective oxidation over supported metal catalysts: From nanoparticles to single atoms. *Appl. Catal. B Environ. Energy* **325**, 122384 (2023).

58. Liu, X. et al. Defect stabilized gold atoms on graphene as potential catalysts for ethylene epoxidation: A first-principles investigation. *Catal. Sci. Technol.* **6**, 1632–1641 (2016).

59. Li, Z. et al. Recent advancements in graphene-based supports of metal complexes/oxides for epoxidation of alkenes. *Chem. Asian J.* **13**, 3790–3799 (2018).

60. Xu, G. et al. Alkali etching of porous PdCoZn nanosheets for boosting C – C bond cleavage of ethylene glycol oxidation. *Small* **20**, 2306341 (2024).

61. Amenabar, I. et al. Hyperspectral infrared nanoimaging of organic samples based on Fourier transform infrared nanospectroscopy. *Nat. Commun.* **8**, 14402 (2017).

62. Kang, J. & Kang, D. Effect of amino acid-derived nitrogen and/or sulfur doping on the visible-light-driven antimicrobial activity of carbon quantum dots: A comparative study. *Chem. Eng. J.* **420**, 129990 (2021).

63. Yu, H., Yu, J., Liu, S. & Mann, S. Template-free hydrothermal synthesis of CuO/Cu_2O composite hollow microspheres. *Chem. Mater.* **19**, 4327–4334 (2007).

64. Zhang, X. et al. Activation of molecular oxygen over Mn-doped La_2CuO_4 perovskite for direct epoxidation of propylene. *Catal. Sci. Technol.* **12**, 2426–2437 (2022).

65. Lei, J. et al. Insight into the effect of copper substitution on the catalytic performance of $LaCoO_3$-based catalysts for direct epoxidation of propylene with molecular oxygen. *ACS Sustain. Chem. Eng.* **9**, 794–808 (2021).

Acknowledgements

Author contributions

Competing interests

The authors declare no competing interests.

Additional information